nature geoscience

ARTICLES

https://doi.org/10.1038/s41561-021-00843-9

Check for updates

Vertical decoupling in Late Ordovician anoxia due to reorganization of ocean circulation

Alexandre Pohl[1,2]✉, Zunli Lu[3]✉, Wanyi Lu[3], Richard G. Stockey[4], Maya Elrick[5], Menghan Li[6], André Desrochers[7], Yanan Shen[6], Ruliang He[3], Seth Finnegan[8] and Andy Ridgwell[1]

Geochemical redox proxies indicate that seafloor anoxia occurred during the latest Ordovician glacial maximum, coincident with the second pulse of the Late Ordovician mass extinction. However, expanded anoxia in a glacial climate strikingly contrasts with the warming-associated Mesozoic anoxic events and raises questions as to both the causal mechanism of ocean deoxygenation and its relationship with extinction. Here we firstly report iodine-to-calcium ratio (I/Ca) data that document increased upper-ocean oxygenation despite the concurrent expansion of seafloor anoxia. We then resolve these apparently conflicting observations as well as their relationship to global climate by means of a series of Earth system model simulations. Applying available Late Ordovician (Hirnantian) sea-surface temperature estimates from oxygen isotope studies as constraints, alongside our I/Ca data, leads us to identify a scenario in which Hirnantian glacial conditions permit both the spread of seafloor anoxia and increased upper-ocean oxygenation. Our simulated mechanism of a reorganization of global ocean circulation, with reduced importance of northern-sourced waters and a poorer ventilated and deoxygenated deep ocean has parallels with Pleistocene state transitions in Atlantic meridional overturning (despite a very different continental configuration) and suggests that no simple and predictable relationship between past climate state and oxygenation may exist.

The Late Ordovician mass extinction (LOME) is the first of the 'Big Five' mass extinctions[1] and was characterized by the disappearance of ~85% of marine species[2]. Extinction clustered in two apparent pulses[2] (Fig. 1): at the beginning (LOME 1) and near the end of the Hirnantian (LOME 2). LOME 1 may be related to habitat loss associated with glacio-eustatically driven sea-level changes or potentially volcanism[2–4], while the drivers responsible for LOME 2 are more debated. In the traditional time-line interpretation, LOME 2 occurred during deglaciation; extinction was then triggered by the expansion of anoxia onto the shelves during the associated sea-level rise[5]. However, recent studies conducted at higher stratigraphic resolution have challenged this model[6,7] and suggested that seafloor anoxia[7] was already well established during the latest Hirnantian glacial maximum[7,8].

The increased areal extent of seafloor anoxia, indicated by $\delta^{238}U$, coincident with glacial conditions rather than global warming, presents several apparent conundrums. Firstly, this is seemingly at odds with the well-established conceptual model for typical Mesozoic ocean anoxic events which links volcanism with greenhouse-driven warming and hence the occurrence of global-scale anoxia[9]. Indeed, previous ocean biogeochemical modelling studies of Hirnantian climate have reported increased oxygenation during glaciation[10], which is an expected corollary of decreased oxygenation during Mesozoic warming episodes[9]. Secondly, despite uranium isotopic evidence for expanded seafloor anoxia globally[7], most preserved stratigraphic sections, deposited at various latitudes in shelf and slope settings, record a shift to more oxic depositional facies during the Hirnantian[11]. How can deep ocean deoxygenation develop in a cold climate, and become decoupled from increased shallow marine oxygenation?

We resolve this conundrum through a series of Earth system model experiments that reveal how state transitions in large-scale ocean circulation in response to Ordovician climate change can lead to a dramatic redox restructuring of the marine environment. However, we start by confirming the existence of surface-to-deep redox decoupling during the latest Ordovician and report the results of carbonate I/Ca measured in two Laurentian sections spanning the late Katian to earliest Silurian (Rhuddanian).

I/Ca data and upper-ocean oxygenation during LOME 2

Bulk carbonate I/Ca (Methods) reflects changes in dissolved iodate (IO_3^-) concentration, which decreases in the presence of low-oxygen water masses[12,13]. Lower I/Ca ratios have been documented previously during Mesozoic warming events[12], providing evidence for the ocean deoxygenation–warming link. Here, results obtained for two Laurentian sections (Extended Data Fig. 1) show increasing mean I/Ca ratios from the middle segment of the Hirnantian Isotope Carbon Excursion (mid HICE) to the late HICE and LOME 2 (Fig. 1 and Extended Data Fig. 2). The higher I/Ca ratios recorded in the Laurentian epicontinental seas (water depths less than ~200 m) suggest that latest Ordovician cooling was contemporaneous with increased oxygenation of the upper ocean, which is independently supported by the Anticosti Island organic biomarker analysis of Rohrssen et al.[14] and is not easily explained as a diagenetic artefact[15,16] (Supplementary Discussion and Extended Data Fig. 3). Furthermore, I/Ca ratios are higher at Anticosti Island (Canada)[7] than at Copenhagen Canyon (USA)[17] during LOME 2 (Fig. 1). This is consistent with Copenhagen Canyon being deposited in predominantly poorly oxygenated offshore waters and closer to the large Laurentian oxygen minimum zone (Extended Data Fig. 1) core as

[1]Department of Earth and Planetary Sciences, University of California, Riverside, CA, USA. [2]Biogéosciences, UMR 6282, UBFC/CNRS, Université Bourgogne Franche-Comté, Dijon, France. [3]Department of Earth Sciences, Syracuse University, Syracuse, NY, USA. [4]Department of Geological Sciences, Stanford University, Stanford, CA, USA. [5]Earth and Planetary Sciences, University of New Mexico, Albuquerque, NM, Mexico. [6]School of Earth and Space Sciences, University of Science and Technology of China, Hefei, China. [7]Earth and Environmental Sciences, University of Ottawa, Ottawa, Ontario, Canada. [8]Department of Integrative Biology, University of California, Berkeley, Berkeley, CA, USA. ✉e-mail: alexandre.pohl@u-bourgogne.fr; zunlilu@syr.edu

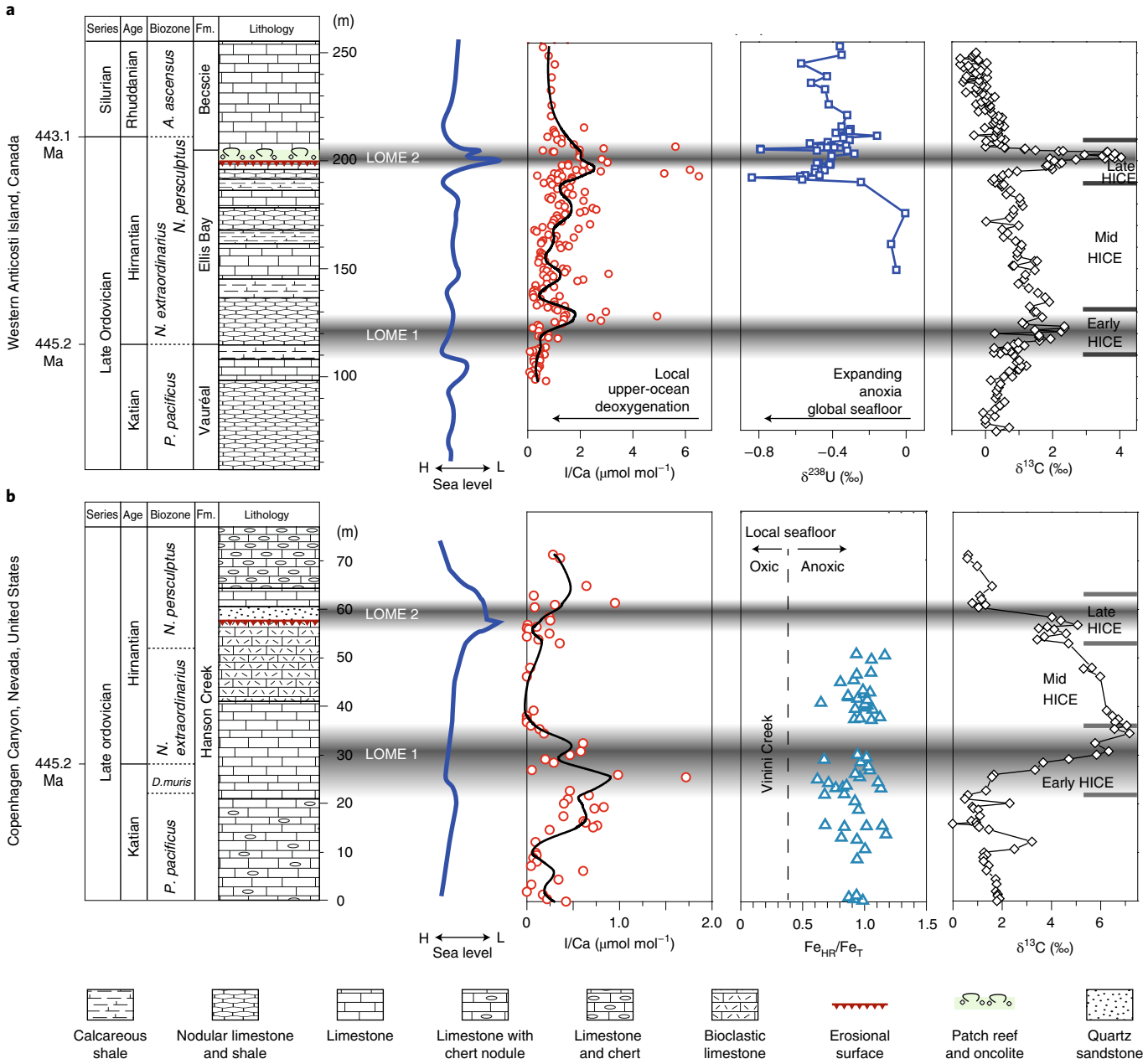

Fig. 1 | Stratigraphic, glacio-eustatic and geochemical records. a,**b**, Results from western Anticosti Island (Quebec, Canada) (**a**) and Copenhagen Canyon (Nevada, United States) (**b**). The I/Ca curves shown with LOESS smoothing are from this study. Note the difference in scale for I/Ca between Anticosti and Copenhagen Canyon. For western Anticosti Island, stratigraphic, sea level, $\delta^{13}C$ and $\delta^{238}U$ data are from refs. [6,7,44]. For Copenhagen Canyon, stratigraphic, sea level and $\delta^{13}C$ data are from refs. [17,45] Highly reactive iron to total iron ratio (Fe_{HR}/Fe_T) data[18] are from a nearby section (Vinini Creek, Nevada). Grey-shaded bands indicate the approximate stratigraphic position of LOME extinctions. Numerical ages are from ref. [46]. Location of each section is shown in Fig. 3 and Extended Data Fig. 1. *Paraorthograptus pacificus* (*P. pacificus*), *Normalograptus extraordinarius* (*N. extraordinarius*), *Normalograptus persculptus* (*N. persculptus*), *Akidograptus ascensus* (*A. ascensus*).

well as with Fe speciation data from Vinini Creek (Nevada) recording local anoxic deep waters in an upwelling setting[18] (Fig. 1).

Two models for seafloor anoxia in a cold climate

To reconcile the various observations of increased seafloor anoxia from uranium isotopes[7] but increased upper-ocean oxygenation from I/Ca, we carry out a gridded parameter ensemble of simulations using the cGENIE Earth system model of intermediate complexity[19] configured with Ordovician continental boundary conditions and reduced (3.65%) Ordovician solar luminosity value (Methods). We simulate a range of plausible Hirnantian climatic conditions by running the model multiple times using different atmospheric pCO_2 values (the first parameter axis in the ensemble), for which we chose a range spanning from ×5 to ×24 pre-industrial (280 ppm) concentrations[20], equivalent to 1,400–6,720 ppm.

In the ocean, it is likely that nutrient inventories were lower than modern as a consequence of reduced (compared with modern) Ordovician plant cover[21] and high sea level[22], both tending to suppress terrestrial weathering and cause lower river nutrient input than today. We therefore also simultaneously considered a range of

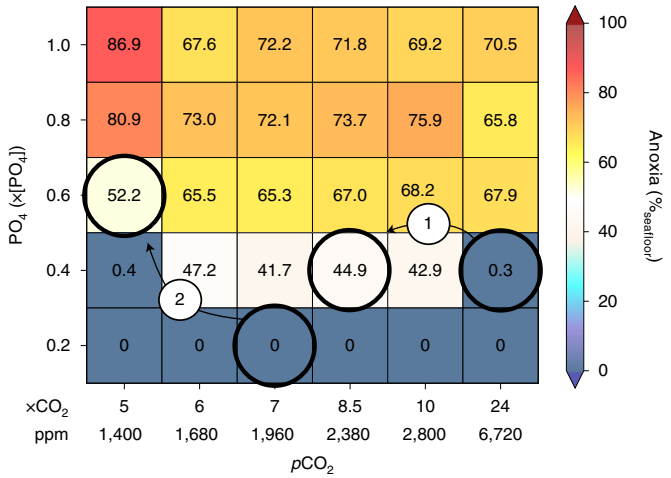

Fig. 2 | Simulated sensitivity of ocean anoxia to climate and marine productivity. Extent of seafloor anoxia (defined as percentage of total seafloor area characterized by benthic ocean $[O_2] \leq 0$ μmol kg^{-1}) as a function of both pCO_2 and ocean PO_4 inventory. Values and colour in each cell represent the extent of anoxia of a single simulation. Arrows and labels represent scenarios 1 and 2, selected to capture the expansion of seafloor anoxia in the latest Hirnantian glacial climate, based on temperature estimates derived respectively from clumped isotopes[26] and $\delta^{18}O_{apatite}$ (refs. [7,27]). Note that pCO_2 values are shown on two scales: ppm and $\times CO_2$ (times the pre-industrial atmospheric concentration of 280 ppm).

ocean dissolved phosphate inventories, from 0.2 to 1.0 times the present-day mean oceanic concentration ($[PO_4]$) of 2.159 μmol kg^{-1} (Fig. 2), which constitutes the second parameter axis of our ensemble. We hence explore a total of 30 different combinations of pCO_2 and ocean phosphate inventory in a regular grid. All simulations were run to steady state (10,000 years), and the ensemble we focus on assumes a reasonable estimate for the Ordovician atmospheric oxygen abundance[23–25] of 8.38%, which is ×0.4 the modern value of 20.95%. Changes in the extent of seafloor anoxia simulated in response to changes in both atmospheric pCO_2 and ocean $[PO_4]$ are shown in Fig. 2.

At ×0.2 $[PO_4]$, the model Ordovician seafloor is fully oxic, regardless of the value of pCO_2 and hence climatic state (Fig. 2). As expected, the extent of seafloor anoxia (defined as benthic $[O_2] \leq 0$ μmol kg^{-1} and the presence of free sulphide (H_2S) in the model) shows a generally positive saturating relationship with increasing phosphate inventory—a direct response of the changing bacterial oxygen demand as biological primary productivity and carbon export to the ocean interior (and the strength of the 'biological pump') increase. In contrast, we find an unexpected and highly non-linear relationship between the extent of seafloor anoxia and pCO_2, with a prominent maximum in percentage anoxia reached for intermediate pCO_2 values (between ×6 and ×10 CO_2) at ×0.4 $[PO_4]$.

To identify a plausible scenario through the climate–productivity space for the cooling climate leading into the Hirnantian glacial maximum (Fig. 2), we first compare modelled surface ocean temperatures with estimates from carbonate clumped isotopes[26] and $\delta^{18}O_{apatite}$ (refs. [7,27]) (Supplementary Results). Hirnantian climate trends are not currently known with sufficient resolution on Anticosti (or elsewhere) to precisely establish the timing of the onset of cooling leading into the late HICE glacial maximum and its relationship with the $\delta^{238}U$ and I/Ca records. We estimate the magnitude of cooling by comparing palaeo-temperatures from the Laframboise Member of the Ellis Bay Formation with those from the lower Ellis Bay Formation. Note that, because the Laframboise Member is interpreted as representing deglacial transgression rather than the glacial maximum[6], our estimated temperature changes are best regarded as minimal. Clumped isotopes suggest a decrease from ca. 33 °C to 29 °C, while $\delta^{18}O_{apatite}$ data suggest a decrease from ca. 30 °C to 23 °C. We use these estimates to posit two end-member possibilities for the associated change in atmospheric pCO_2 within the model ensemble: a drop from ×24 to ×8.5 CO_2[26] (cooling scenario 1) or a drop from ×7 to ×5 CO_2 (refs. [7,27]) (cooling scenario 2).

Next, and with these two plausible cooling scenarios in mind, we seek to constrain pairs of simulations that are characterized by an appropriate expansion of seafloor anoxia in the cold climatic state. Mass balance modelling of the late Hirnantian negative carbonate $\delta^{238}U$ excursion at Anticosti Island[7] permits us to refine the estimate of anoxia extent by accounting for the marine uranium budget[28] and indicates a shift from near-modern levels of ocean oxygenation (<1% seafloor area anoxic)[7,8] to anywhere from 3% to 80% total anoxic seafloor area[8] (Extended Data Fig. 4 and Supplementary Results). We can hence further refine our choice of model simulations to pairs in which the extent of seafloor anoxia is initially (in the warm state) close to modern but is substantially expanded in the cold state.

As illustrated in Fig. 2 (and Extended Data Fig. 5), for scenario 1 (a pCO_2 drop from ×24 to ×8.5 CO_2), we identify a pair of model experiments consistent with our criteria for anoxia expansion (in this case, from ca. 0% to 45% of seafloor area) at a constant nutrient inventory of ×0.4 $[PO_4]$. For scenario 2 (pCO_2 decreasing from ×7 to ×5 CO_2), an increase in ocean phosphate is required in addition to the cooling in order to trigger deep-ocean deoxygenation. We identify an increase from ×0.2 to ×0.6 $[PO_4]$ as consistent with our criteria for seafloor anoxia expansion (Fig. 2 and Extended Data Fig. 5). The possibility of an increase in ocean nutrient inventory is supported by models and experiments suggesting that colonization of the continents by (non-)vascular[29] land plants could have driven a substantial increase in phosphorus weathering flux during the Hirnantian[21,30]. Additional simulations run under alternative assumptions of atmospheric pO_2 (Extended Data Fig. 6) reveal that these nutrient scenarios are not unique, and that different combinations of pO_2 and ocean phosphate inventory may produce similar modelled values of seafloor anoxia. However, the major distinction between the two scenarios remains the same: cooling alone triggers the expansion of seafloor anoxia in scenario 1, while cooling in scenario 2 requires a simultaneous increase in ocean nutrient inventory.

Reconciling shallow- and deep-marine oxygenation trends

To distinguish between the two model scenarios, we now turn to evidence for upper-ocean oxygenation changes. A key difference between scenarios 1 and 2 is the change in the oxygen concentrations simulated in the upper ocean (Fig. 3). In scenario 1, oxygen concentrations in the upper ocean increase in response to climate cooling because oxygen solubility increases in colder water[10,31] while the metabolic rates of marine organisms, and thus primary productivity, decrease[32]. The rate at which particulate organic matter is degraded in the ocean interior also decreases in response to lower temperatures[32,33], with less remineralization (and hence oxygen demand) occurring in the upper water column, leaving a relatively larger flux to be consumed at greater depths. A more efficient (deeper-penetrating) biological pump also reduces the return nutrient flux to the ocean surface, further lowering primary productivity (Methods and Supplementary Results). In contrast, for scenario 2, upper-ocean (subsurface) oxygen concentrations decrease primarily as a consequence of a dominant nutrient inventory-driven enhancement of the biological pump which overwhelms the effects of cooling (Supplementary Results). Our I/Ca measurements then distinguish between the two scenarios and identify scenario 1 as best capturing the overall Hirnantian ocean redox changes, with the spread of seafloor anoxia[7] paired with increased oxygenation of the upper ocean (Fig. 1).

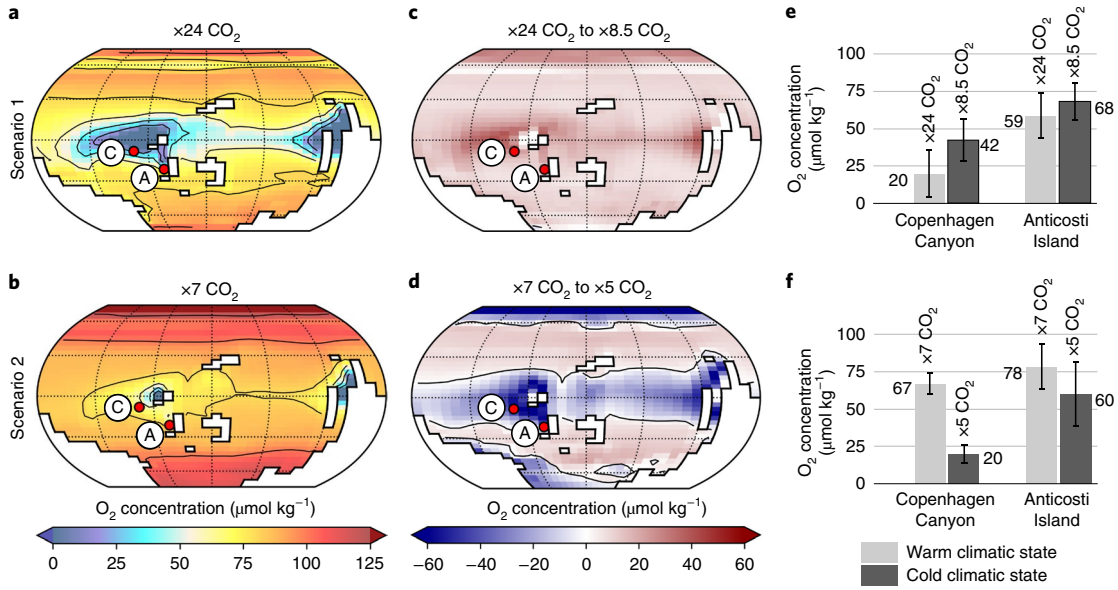

Fig. 3 | Upper-ocean oxygen concentrations. a,**b**, Ocean oxygen concentration simulated between 80 and 175 m water depth (that is, the subsurface grid level in the ocean model) before cooling in scenario 1 (**a**; ×24 CO_2; ×1 CO_2 = 280 ppm) and 2 (**b**; ×7 CO_2). **c**,**d**, Impact of cooling on ocean oxygenation at the same water depth in each scenario, showing emerged landmasses (shaded white and contoured with a thick black line) and palaeo-locations of Anticosti Island (A) and Copenhagen Canyon (C) (red dots) (Fig. 1) for scenario 1 (**c**) and 2 (**d**). **e**,**f**, Oxygen concentration simulated at Anticosti and Copenhagen Canyon before (light grey) and after (dark grey) cooling in scenario 1 (**e**) and 2 (**f**). Error bars show ±1 s.d., calculated based on all oceanic neighbouring points in the model.

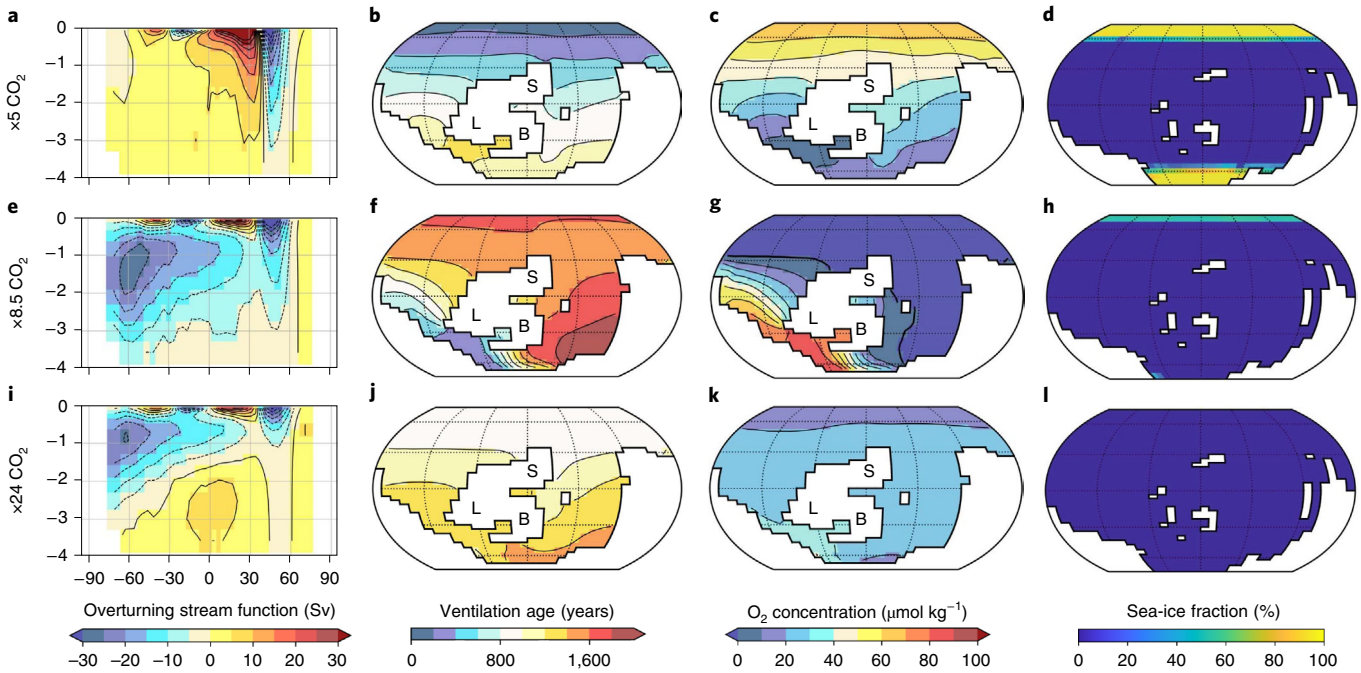

Fig. 4 | Ocean circulation response to cooling. a–**l**, Meridional overturning circulation (**a**,**e**,**i**; 1 Sv = 10^6 m^3 s^{-1}), deep-ocean ventilation age simulated at ca. 3,900 m water depth (**b**,**f**,**j**), deep-ocean oxygen concentration simulated at ca. 3,900 m water depth (**c**,**g**,**k**) and mean annual sea-ice fraction (**d**,**h**,**l**), simulated using pCO_2 of ×5 (**a**–**d**), ×8.5 (**e**–**h**) and ×24 (**i**–**l**) (×1 CO_2 = 280 ppm). Results in **c**,**g**,**k** obtained at ×0.4 pO_2 and ×0.4 [PO_4]. In **a**,**e**,**i**, positive (negative) values in the meridional overturning circulation represent clockwise (anticlockwise) cells. The ventilation age represents the time since a parcel of water last reached the ocean surface. L, Laurentia; B, Baltica; S, Siberia.

By applying multiple data constraints to an ensemble of different realizations of Ordovician climate and marine biogeochemical cycle states, we can reconcile the divergent trends in seafloor and upper-ocean oxygenation in response to ongoing global cooling. In the model, we account for the observations as a result of a fundamental reorganization occurring in large-scale ocean circulation patterns. In the warmest ×24 CO_2 state, deep-water formation in the model predominantly occurs at the highest ocean latitudes (which

in the Late Ordovician were located in the Northern Hemisphere) and ventilates much of the Ordovician seafloor (Fig. 4i–l). As pCO_2 is lowered through to ×8.5, seasonal sea ice appears over the North Pole (Fig. 4e–h). Seasonal freshwater fluxes associated with retreating sea-ice cover locally stratify and thus stabilize the water column (Supplementary Results). This mechanism, possibly strengthened by a positive feedback between reduced northwards salinity transport and deep-water formation and hence overturning, leads to a shutdown of deep-water formation over the North Pole. Although Southern Hemisphere overturning strengthens, this is restricted to the west of the low-latitude Laurentia and Baltica continents and leaves much of the ocean floor (particularly to the east of Laurentia and Baltica) poorly ventilated (Fig. 4f,g). We find support for such a shift in large-scale ocean circulation occurring in response to cooling in the higher-resolution MITgcm study of Pohl et al.[10]. Despite using a different continental reconstruction of the Late Ordovician[34], they found a shut-down of northern-sourced deep water in response to a reduction in the solar constant and cooling, with a similar change in the pattern of global overturning (Supplementary Results) and a restriction of southern-sourced oxygenation to the west of Laurentia and Baltica. More idealized basin geometry (and coincidently also using MITgcm) modelling also demonstrates the potential for abrupt transitions in meridional overturning circulation, and Rose et al.[35] find this specifically in response to the incipient growth of polar sea-ice cover. Regardless, further work using coupled climate models that can account for the potential role of inter-annual variability and ocean–atmosphere modes in the state dependence of large-scale circulation patterns in the Ordovician (that we are unable to address with the cGENIE model) is important and would help identify which modes of Late Ordovician ocean circulation are robust (and which might be model dependent) and how they respond to climate change.

We suggest that a helpful analogy for better visualizing the Ordovician circulation and oxygenation changes that occur in our model between ×24 and ×8.5 pCO_2 (scenario 1) can be found during the glacial–interglacial cycles of the Late Pleistocene. Specifically, we note how northern-sourced, deep-water production in the Atlantic decreases as climate cools (and is replaced at depth by deep water sourced from the south)[36], with the potential for multiple circulation states with abrupt transitions between them[35,37]. Furthermore, shallowing of the Atlantic meridional overturning circulation coincides with proxy evidence for reduced oxygenation at depth, despite glacial deep-ocean temperatures being colder than during interglacials[38,39].

Finally, an important conclusion we draw from our I/Ca data and simulations is that increased seafloor anoxia is, by itself, an insufficient explanation for LOME 2. There is no evidence of reduced local upper-ocean oxygenation associated with LOME 2 at Anticosti. If anything, there is evidence of increased oxygenation based on I/Ca at this time (Fig. 1). The majority of Anticosti taxonomic last occurrences also occur above the onset of the negative uranium isotope excursion[40,41], and globally many of the taxa that disappeared during LOME 2 occurred primarily in shallow-water habitats that would have remained well oxygenated under almost any reasonable global change scenario. Thus, we suggest that cooling must have interacted with other factors such as changes in nutrient cycling and primary producer communities[11,42], and potentially heavy-metal toxicity[43], to drive the LOME 2 extinction.

Online content

Any methods, additional references, Nature Research reporting summaries, source data, extended data, supplementary information, acknowledgements, peer review information; details of author contributions and competing interests; and statements of data and code availability are available at https://doi.org/10.1038/s41561-021-00843-9.

Received: 20 August 2020; Accepted: 17 September 2021;
Published online: 01 November 2021

References

1. Sepkoski, J. J., Bambach, R. K., Raup, D. M. & Valentine, J. W. Phanerozoic marine diversity and the fossil record. *Nature* **293**, 435–437 (1981).
2. Harper, D. A. T., Hammarlund, E. U. & Rasmussen, C. M. Ø. End Ordovician extinctions: a coincidence of causes. *Gondwana Res.* **25**, 1294–1307 (2013).
3. Saupe, E. et al. Extinction intensity during Ordovician and Cenozoic glaciations explained by cooling and palaeogeography. *Nat. Geosci.* **13**, 65–70 (2019).
4. Hu, D. et al. Large mass-independent sulphur isotope anomalies link stratospheric volcanism to the Late Ordovician mass extinction. *Nat. Commun.* **11**, 2297 (2020).
5. Holmden, C. et al. Nd isotope records of late Ordovician sea-level change—Implications for glaciation frequency and global stratigraphic correlation. *Palaeogeogr. Palaeoclimatol. Palaeoecol.* **386**, 131–144 (2013).
6. Ghienne, J.-F. et al. A Cenozoic-style scenario for the end-Ordovician glaciation. *Nat. Commun.* **5**, 4485 (2014).
7. Bartlett, R. et al. Abrupt global-ocean anoxia during the Late Ordovician–early Silurian detected using uranium isotopes of marine carbonates. *Proc. Natl Acad. Sci. USA* **115**, 5896–5901 (2018).
8. Stockey, R. G. et al. Persistent global marine euxinia in the early Silurian. *Nat. Commun.* **11**, 1804 (2020).
9. Jenkyns, H. C. Geochemistry of oceanic anoxic events. *Geochem. Geophys. Geosyst.* **11**, Q03004 (2010).
10. Pohl, A., Donnadieu, Y., Le Hir, G. & Ferreira, D. The climatic significance of Late Ordovician–early Silurian black shales. *Paleoceanography* **32**, 397–423 (2017).
11. Melchin, M. J., Mitchell, C. E., Holmden, C. & Štorch, P. Environmental changes in the Late Ordovician–early Silurian: review and new insights from black shales and nitrogen isotopes. *Geol. Soc. Am. Bull.* **125**, 1635–1670 (2013).
12. Lu, Z., Jenkyns, H. C. & Rickaby, R. E. M. Iodine to calcium ratios in marine carbonate as a paleo-redox proxy during oceanic anoxic events. *Geology* **38**, 1107–1110 (2010).
13. Lu, Z. et al. Oxygen depletion recorded in upper waters of the glacial Southern Ocean. *Nat. Commun.* **7**, 11146 (2016).
14. Rohrssen, M., Love, G. D., Fischer, W., Finnegan, S. & Fike, D. A. Lipid biomarkers record fundamental changes in the microbial community structure of tropical seas during the Late Ordovician Hirnantian glaciation. *Geology* **41**, 127–130 (2013).
15. Hardisty, D. S. et al. Perspectives on Proterozoic surface ocean redox from iodine contents in ancient and recent carbonate. *Earth Planet. Sci. Lett.* **463**, 159–170 (2017).
16. Jones, D. S. et al. Sea level, carbonate mineralogy, and early diagenesis controlled δ13C records in Upper Ordovician carbonates. *Geology* **48**, 194–199 (2020).
17. Hu, D. et al. $^{87}Sr/^{86}Sr$ evidence from the epeiric Martin Ridge Basin for enhanced carbonate weathering during the Hirnantian. *Sci. Rep.* **7**, 11348 (2017).
18. Ahm, A.-S. C., Bjerrum, C. J. & Hammarlund, E. U. Disentangling the record of diagenesis, local redox conditions, and global seawater chemistry during the latest Ordovician glaciation. *Earth Planet. Sci. Lett.* **459**, 145–156 (2017).
19. Ridgwell, A. et al. Marine geochemical data assimilation in an efficient Earth system model of global biogeochemical cycling. *Biogeosciences* **4**, 87–104 (2007).
20. Berner, R. A. GEOCARBSULF: a combined model for Phanerozoic atmospheric O_2 and CO_2. *Geochim. Cosmochim. Acta* **70**, 5653–5664 (2006).
21. Porada, P. et al. High potential for weathering and climate effects of non-vascular vegetation in the Late Ordovician. *Nat. Commun.* **7**, 12113 (2016).
22. Scotese, C. R. & Wright, N. *PALEOMAP Paleodigital Elevation Models (PaleoDEMS) for the Phanerozoic* (PALEOMAP Project, 2018); https://www.earthbyte.org/paleodem-resource-scotese-and-wright-2018/
23. Lenton, T. M., Daines, S. J. & Mills, B. J. W. COPSE reloaded: an improved model of biogeochemical cycling over Phanerozoic time. *Earth Sci. Rev.* **178**, 1–28 (2018).
24. Lu, W. et al. Late inception of a resiliently oxygenated upper ocean. *Science* **5**, eaar5372 (2018).
25. Sperling, E. A. et al. Statistical analysis of iron geochemical data suggests limited late Proterozoic oxygenation. *Nature* **523**, 451–454 (2015).
26. Finnegan, S. et al. The magnitude and duration of late Ordovician–early Silurian glaciation. *Science* **331**, 903–906 (2011).
27. Trotter, J. A., Williams, I. S., Barnes, C. R., Lécuyer, C. & Nicoll, R. S. Did cooling oceans trigger Ordovician biodiversification? Evidence from conodont thermometry. *Science* **321**, 550–554 (2008).

28. Zhang, F. et al. Uranium isotopes in marine carbonates as a global ocean paleoredox proxy: a critical review. *Geochim. Cosmochim. Acta* **287**, 27–49 (2020).
29. Steemans, P. et al. Origin and radiation of the earliest vascular land plants. *Science* **324**, 353 (2009).
30. Lenton, T. M., Crouch, M., Johnson, M., Pires, N. & Dolan, L. First plants cooled the Ordovician. *Nat. Geosci.* **5**, 86–89 (2012).
31. Garcia, H. E. & Gordon, L. I. Oxygen solubility in seawater: better fitting equations. *Limnol. Oceanogr.* **37**, 1307–1312 (1992).
32. Crichton, K. A., Wilson, J. D., Ridgwell, A. & Pearson, P. N. Calibration of temperature-dependent ocean microbial processes in the cGENIE.muffin (v0.9.13) Earth system model. *Geophys. Model Dev.* **14**, 125–149 (2021).
33. John, E. H., Wilson, J. D., Pearson, P. N. & Ridgwell, A. Temperature-dependent remineralization and carbon cycling in the warm Eocene oceans. *Palaeogeogr. Palaeoclimatol. Palaeoecol.* **413**, 158–166 (2014).
34. Torsvik, T. H. *BugPlates: Linking Biogeography and Palaeogeography Software Installation* (CEED, 2012); https://www.earthdynamics.org/software/Bugs2_SoftwareManual.pdf
35. Rose, B. E. J., Ferreira, D. & Marshall, J. The role of oceans and sea ice in abrupt transitions between multiple climate states. *J. Clim.* **26**, 2862–2879 (2013).
36. Adkins, J. F. The role of deep ocean circulation in setting glacial climates. *Paleoceanography* **28**, 539–561 (2013).
37. Ferreira, D., Marshall, J., Ito, T. & McGee, D. Linking glacial–interglacial states to multiple equilibria of climate. *Geophys. Res. Lett.* **45**, 9160–9170 (2018).
38. Jaccard, S. L. & Galbraith, E. D. Large climate-driven changes of oceanic oxygen concentrations during the last deglaciation. *Nat. Geosci.* **5**, 151–156 (2012).
39. Lu, W. et al. I/Ca in epifaunal benthic foraminifera: a semi-quantitative proxy for bottom water oxygen in a multi-proxy compilation for glacial ocean deoxygenation. *Earth Planet. Sci. Lett.* **533**, 116055 (2020).
40. Delabroye, A. & Vecoli, M. The end-Ordovician glaciation and the Hirnantian Stage: a global review and questions about Late Ordovician event stratigraphy. *Earth Sci. Rev.* **98**, 269–282 (2010).
41. McCracken, A. D. & Barnes, C. R. Conodont biostratigraphy and paleoecology of the Ellis Bay Formation, Anticosti Island, Quebec, with special reference to Late Ordovician–Early Silurian chronostratigraphy and the systemic boundary. *Bull. Geol. Survey. Can.* **329**, 51–134 (1981).
42. Sheets, H. D. et al. Graptolite community responses to global climate change and the late ordovician mass extinction. *Proc. Natl Acad. Sci. USA* **113**, 8380–8385 (2016).
43. Vandenbroucke, T. R. A. et al. Metal-induced malformations in early Palaeozoic plankton are harbingers of mass extinction. *Nat. Commun.* **6**, 1–7 (2015).
44. Desrochers, A. et al. A far-field record of the end Ordovician glaciation: the Ellis Bay Formation, Anticosti Island, Eastern Canada. *Palaeogeogr. Palaeoclimatol. Palaeoecol.* **296**, 248–263 (2010).
45. Finney, S. C., Berry, W. B. N., Cooper, J. D. & Ripperdan, R. L. Late Ordovician mass extinction: a new perspective from stratigraphic sections in central Nevada. *Geology* **27**, 215–218 (1999).
46. Goldman, D. et al. in *Geologic Time Scale 2020* (eds. Gradstein, F. M., Ogg, J. G., Schmitz, M. D. & Ogg, G. M.) 631–694 (Elsevier, 2020).

Methods

Description of the model. Simulations were conducted using the Earth system model of intermediate complexity cGENIE[19] (Supplementary Methods). cGENIE is rooted in a 3D ocean circulation model, but for speed, includes only a 2D energy–moisture–balance atmospheric component plus sea-ice module. The model was configured on a 36 × 36 equal-area grid with 16 unevenly spaced vertical levels in the ocean. The cycling of carbon and associated tracers in the ocean is based on a single (phosphate) nutrient limitation of biological productivity following Reinhard et al.[47] but adopts the Arrhenius-type temperature-dependent scheme for the remineralization of organic matter exported to the ocean interior of John et al.[33]. Compared with recent Earth system models of the Coupled Model Intercomparison Project phase 6, the simplified climatic component of cGENIE offers a rapid model integration time, facilitating the numerous sensitivity tests required to quantify the impact of the uncertainty in the model boundary conditions pervading deep-time studies, as well as the 10,000-year-long model simulations necessary to ensure deep-ocean equilibrium (Supplementary Results).

Description of the numerical experiments. We adopted the Hirnantian (445 Ma) continental reconstruction of Scotese and Wright[22] (Extended Data Fig. 1). In the absence of better constraints, a flat bottom ocean floor was used, which is not expected to significantly impact simulated global benthic ocean oxygenation patterns[48] (Supplementary Methods). We calculated solar luminosity at 445 Ma (1,318.1 W m^{-2}) after Gough[49], and employed a null eccentricity-minimum obliquity orbital configuration, which provides an equal mean annual insolation to both hemispheres with minimum seasonal contrasts. For each different atmospheric pCO_2 assumption, we first ran the Fast Ocean Atmosphere Model[50] for 2 kyr using these boundary conditions (Supplementary Methods). We then derived the 2D wind speed and wind stress, and 1D zonally averaged albedo forcing fields required by the cGENIE model, using the 'muffingen' open-source software version v0.9.20 (https://doi.org/10.5281/zenodo.4615664).

cGENIE model simulations were initialized with a sea-ice-free ocean and homogeneous temperature and salinity in the ocean (5 °C and 34.9‰, respectively). The model was then integrated for 10,000 years until equilibrium of the deep-ocean oxygen concentration. Results of the mean of the last simulated year were used for this analysis.

Materials and I/Ca methods. Samples from two Upper Ordovician sections were analysed for I/Ca, taken from Anticosti Island, Quebec, Canada and Copenhagen Canyon, Nevada, United States (Supplementary Methods). Rock samples were crushed and homogenized to fine powder. Around 4 mg of powdered samples was weighed and rinsed with de-ionized water to remove soluble iodine. Nitric acid (3%) was added to dissolve carbonate. The samples were then diluted to a consistent matrix containing ~50 ppm Ca, 0.5% tertiary amine (to stabilize iodine) and 5 ppb In and Cs (internal standards). The measurements were performed immediately by quadrupole inductively coupled plasma mass spectrometry (Bruker M90) at Syracuse University. Iodine calibration standards were prepared daily from KIO_3 powder. The sensitivity of iodine was tuned to 80–100 kcps for a 1 ppb standard. The reference standard JCp-1 was analysed repeatedly to monitor long-term accuracy[12,24]. The detection limit of I/Ca is on the order of 0.1 μmol mol^{-1}.

Data availability

The I/Ca data can be downloaded from Zenodo (https://zenodo.org/record/5136966#.YP5vClMzbu6).

Code availability

The code for the version of the 'muffin' release of the cGENIE Earth system model used in this paper is tagged as v0.9.20 and available at https://doi.org/10.5281/zenodo.4618203.

Configuration files for the specific experiments presented in the paper can be found in the directory: genie-userconfigs/MS/pohletal.NatGeo.2020. Details on the experiments, plus the command line needed to run each one, are given in the readme.txt file in that directory. All other configuration files and boundary conditions are provided as part of the code release.

A manual detailing code installation, basic model configuration, tutorials covering various aspects of model configuration and experimental design, plus results output and processing, are available at https://doi.org/10.5281/zenodo.4615662.

References

47. Reinhard, C. T. Oceanic and atmospheric methane cycling in the cGENIE Earth system model. *Geosci. Model Dev.* **13**, 5687–5706 (2020).
48. Osen, A. K., Winguth, A. M. E., Winguth, C. & Scotese, C. R. Sensitivity of Late Permian climate to bathymetric features and implications for the mass extinction. *Glob. Planet. Change* **105**, 171–179 (2013).
49. Gough, D. O. Solar interior structure and luminosity variations*. *Sol. Phys.* **74**, 21–34 (1981).
50. Jacob, R. L. *Low Frequency Variability in a Simulated Atmosphere–Ocean System* (Univ. of Wisconsin Madison, 1997).

Acknowledgements

This project has received funding from the European Union's Horizon 2020 research and innovation programme under the Marie Skłodowska-Curie grant agreement no. 838373 (to A.P.), from NSF EAR-2121445, NSF EAR-1349252, OCE-1232620 and OCE-1736542 (to Z.L.), from the Natural Sciences and Engineering Research Council of Canada (NSERC Discovery Grant) and NSF 17-536 (to A.D.), from the David and Lucile Packard Foundation (to S.F.), from NSF grants 1736771 and EAR-2121165 and the Heising-Simons Foundation (2015-145) (to A.R.) and from the National Natural Science Foundation of China (41520104007, 41721002) (to Y.S. and M.L). Calculations were partly performed using HPC resources from the Centre de Calcul de l'Université de Bourgogne of Direction du Numérique.

Author contributions

A.P., Z.L. S.F. and A.R. designed the study and wrote the manuscript with input from all co-authors. A.P. conducted the Fast Ocean Atmosphere Model and cGENIE experiments and led the analysis of the model results. Z.L., W.L. and R.H. carried out the I/Ca measurements. Z.L. led the analysis of the I/Ca results. R.G.S. conducted the mass balance modelling of the uranium isotope cycle.

Competing interests

The authors declare no competing interests.

Additional information

Extended data is available for this paper at https://doi.org/10.1038/s41561-021-00843-9.

Supplementary information The online version contains supplementary material available at https://doi.org/10.1038/s41561-021-00843-9.

Correspondence and requests for materials should be addressed to Alexandre Pohl or Zunli Lu.

Peer review information *Nature Geoscience* thanks Michael Melchin, Daniel Horton and the other, anonymous, reviewer(s) for their contribution to the peer review of this work. Primary Handling Editor(s): James Super.

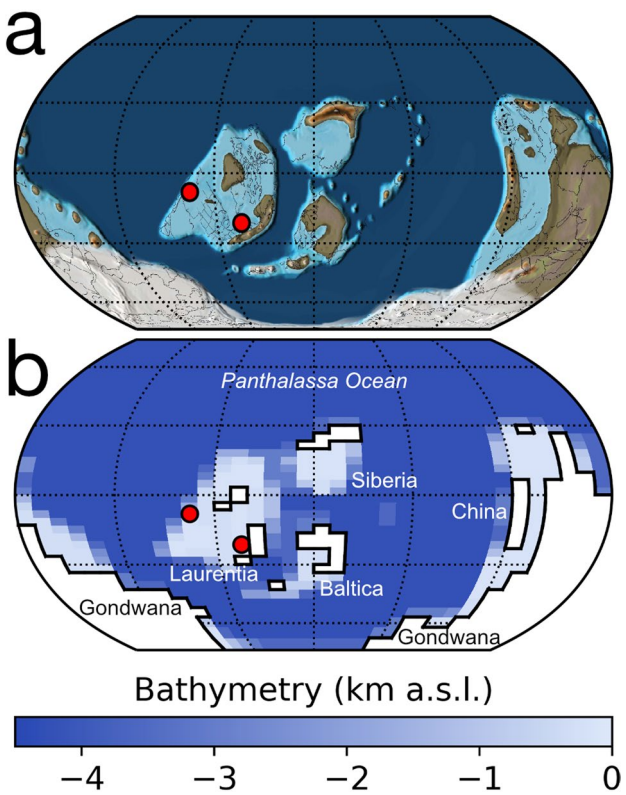

Extended Data Fig. 1 | Latest Ordovician paleogeography. (a) Latest Ordovician (445 Ma) reconstruction of Scotese and Wright[22]. (b) Bathymetry used in the cGENIE simulations, derived from (a). In the absence of a better estimate, the deep ocean is a flat bottom (ca. –4200 m). Names of the main continental masses and the Panthalassa Ocean are indicated on the map. Red dots show the location of the 2 sedimentary sections discussed in the text, where I/Ca data have been collected. *km a.s.l.*: *km above sea level*.

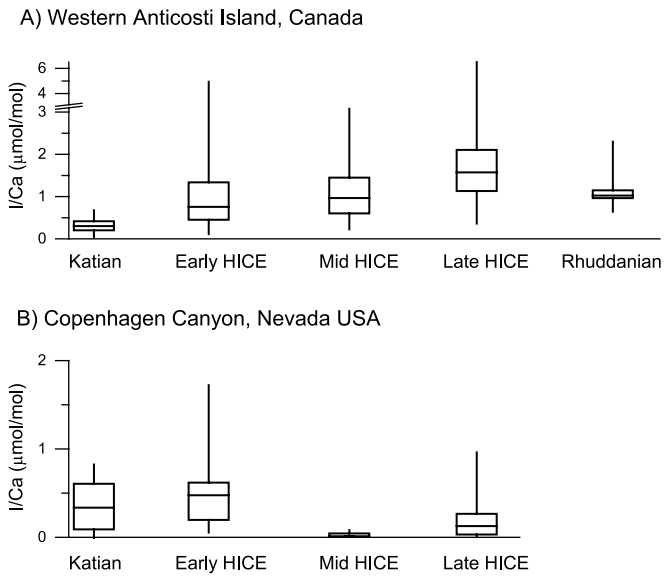

Extended Data Fig. 2 | Box and whisker plot of I/Ca in the Late Ordovician and early Silurian. Boxes mark the 25th and 75th percentiles of values at each time frame, horizontal lines in the box represent the median, and the whiskers show the maximum and minimum. See Fig. 1 for the age of each box and whisker plot. Two-group Mann-Whitney test indicates that I/Ca values in mid HICE versus late HICE are significantly different (p =2.3E-5 for Anticosti Island; p = 0.014 for Copenhagen Canyon).

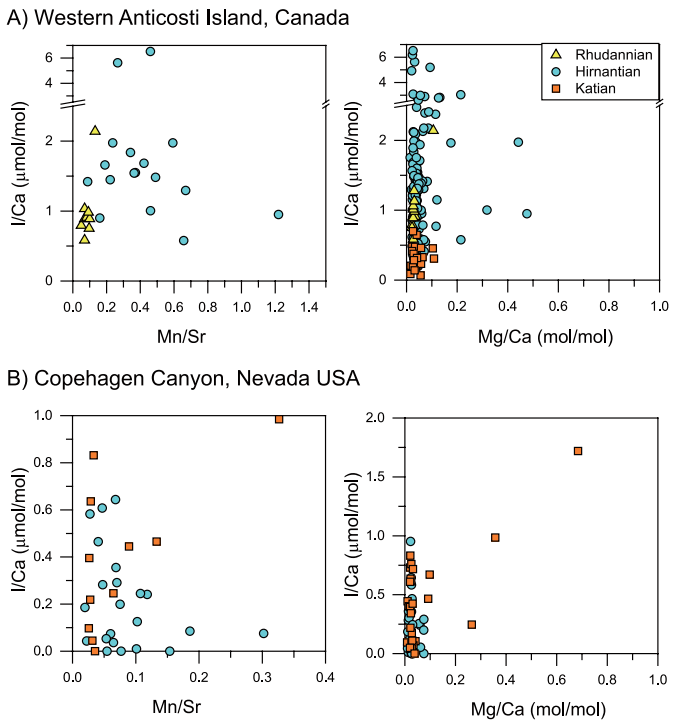

Extended Data Fig. 3 | Cross-plot of I/Ca vs. Mn/Sr and Mg/Ca. Mn/Sr data are from refs. [7,17].

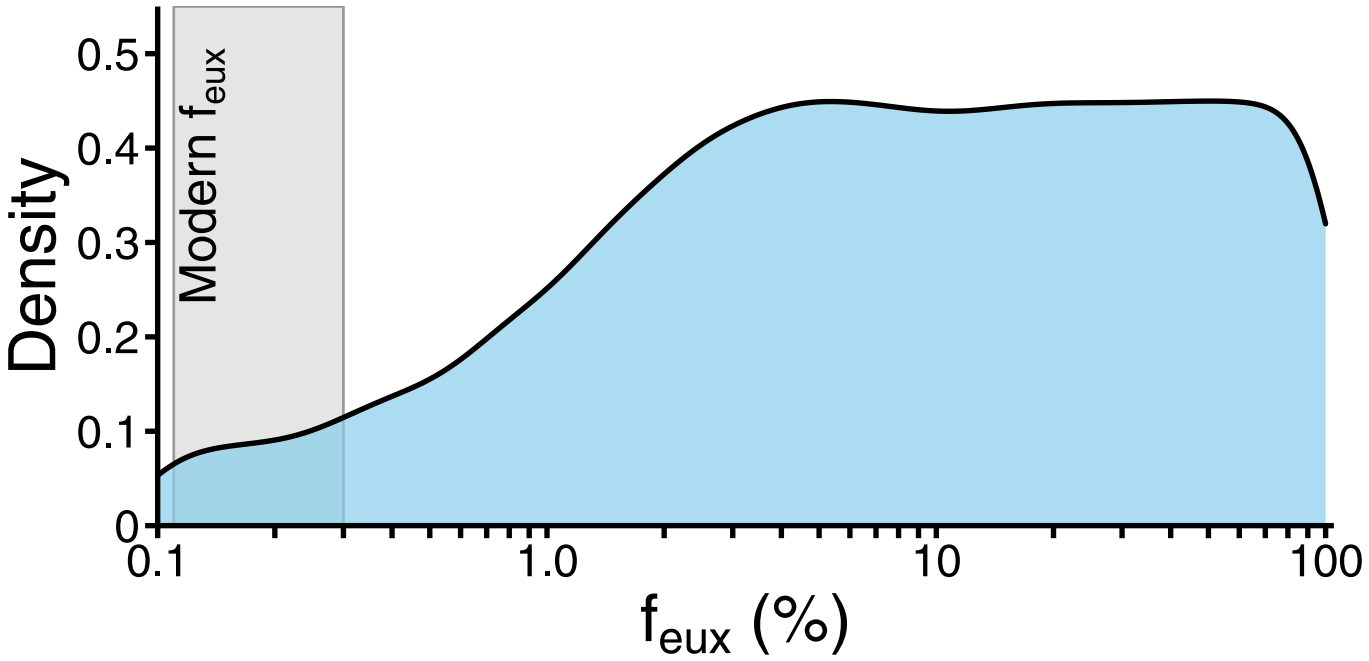

Extended Data Fig. 4 | Density plot illustrating the distribution of f_{eux} values (the fraction of global seafloor with euxinic bottom-waters) compatible with carbonate $\delta^{238}U$ data from the Hirnantian-Rhuddanian ocean anoxic event[7], using a stochastic, three-sink mass balance model[8]. In this study we treat these estimates of euxinia as synonymous with anoxia, both due to limited understanding of uranium cycling in ferruginous environments and the lack of complex iron cycling in the current configuration of cGENIE.

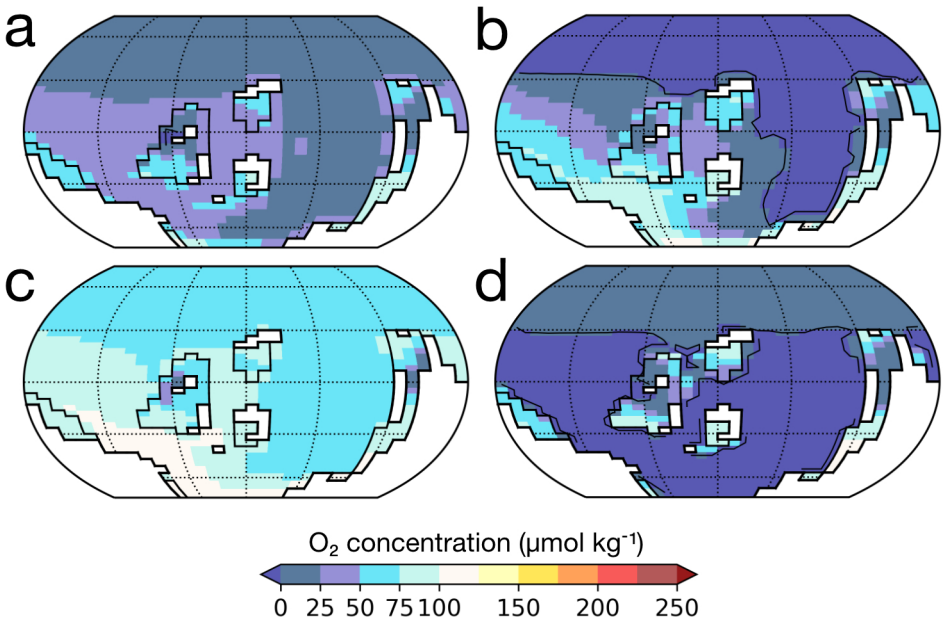

Extended Data Fig. 5 | Seafloor oxygen concentration simulated using an atmospheric pO_2 of ×0.4 and pCO_2 and PO_4 inventory values of respectively (a) ×24 CO_2 and ×0.4 [PO_4], (b) ×8.5 CO_2 and ×0.4 [PO_4], (c) ×7 CO_2 and ×0.2 [PO_4] and (d) ×5 CO_2 and ×0.6 [PO_4]. Shifts from (a) to (b) and from (c) to (d) respectively represent Scenarios #1 and #2 (see Fig. 2). Emerged landmasses are shaded white and contoured with a thick black line. Shallow-water platforms are contoured with a thick black line. Seafloor oxygen concentration here represents the oxygen concentration simulated, for each point of the model grid, in the deepest ocean level. It does not represent the oxygen concentration at any given depth in the model but a draped benthic surface.

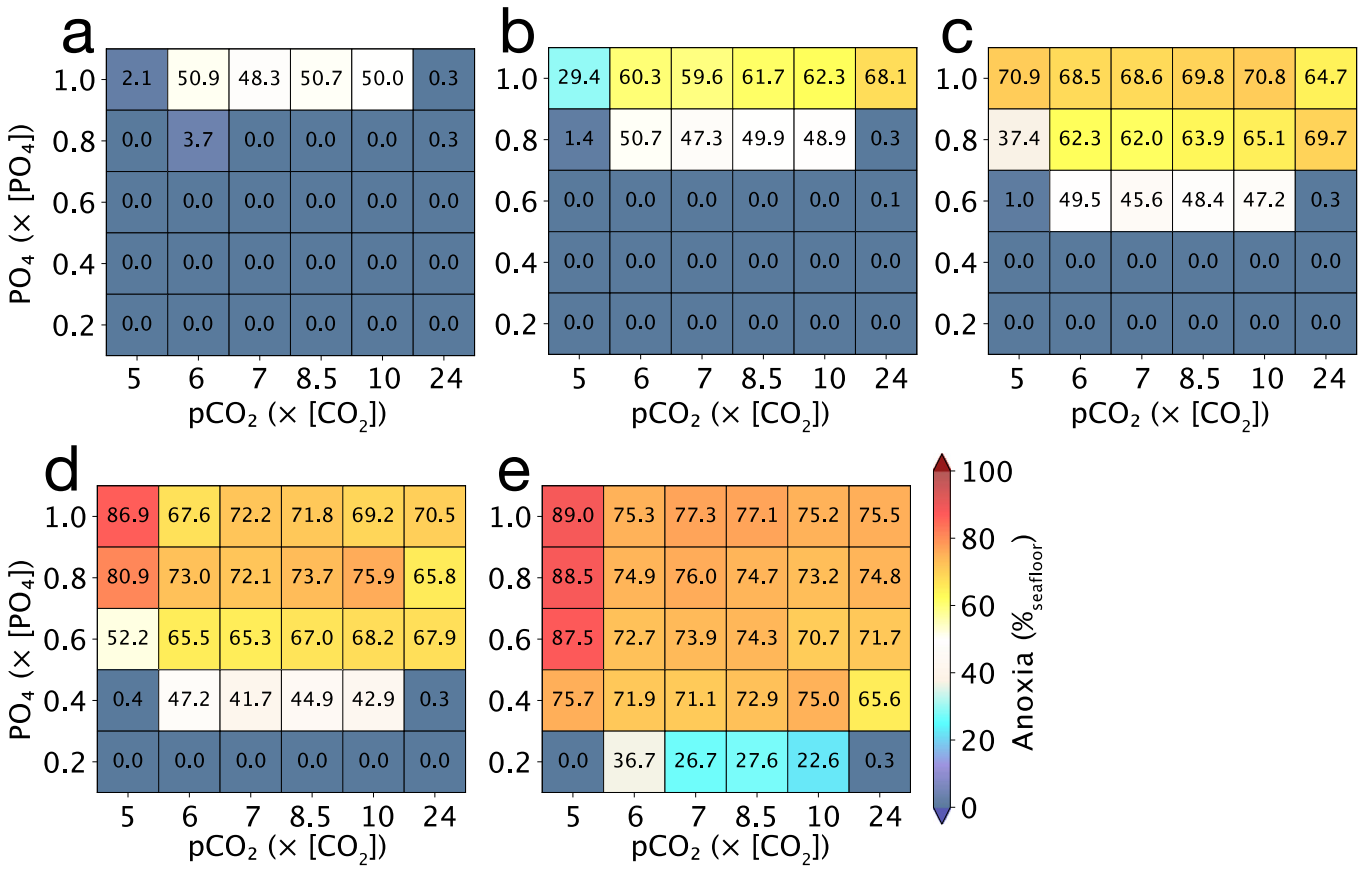

Extended Data Fig. 6 | Extent of seafloor anoxia (defined as percentage of the total seafloor area characterized by a benthic ocean $[O_2] \leq 0$ µmol kg^{-1}) simulated as a function of pCO_2 (x-axis) and ocean PO_4 inventory (y-axis), for pO_2 levels of (a) ×1.0, (b) ×0.8, (c) ×0.6, (d) ×0.4 and (e) ×0.2. Each cell is a cGENIE simulation. Values inside each cell and the colormap both represent the extent of anoxia.